



# Effect of Annealing on the Cavitation Erosion Resistance of HVOF-Sprayed Fe-Based Amorphous Composite Coatings

Jiewen Wang<sup>1,2</sup> · Rui Yang<sup>2</sup> · Ye Tian<sup>2</sup> · Ping Zhou<sup>2</sup> · Jing Huang<sup>2</sup> · Hua Li<sup>1,2</sup> · Xiuyong Chen<sup>2</sup>

Submitted: 7 February 2023 / in revised form: 19 April 2023 / Accepted: 23 April 2023 / Published online: 8 May 2023  
© ASM International 2023

**Abstract** Fe-based amorphous composite coatings were deposited onto 316L stainless steels by high-velocity oxygen-fuel spraying. Some of the coatings were annealed at 600 or 850 °C for 1 h in a vacuum. The cavitation erosion test was conducted in deionised water (DW) and artificial seawater (AS) to study the effect of annealing on the cavitation erosion resistance of the coatings. Mechanical properties and corrosion resistance were also investigated. The study revealed that the 850 °C annealed coating exhibited the best cavitation erosion resistance in both DW and AS despite compromised corrosion resistance due to the crystalline growth by annealing. The reduced porosity and increased fracture toughness of the coating after annealing at 850 °C contributed to the improved cavitation erosion resistance. In addition, the transformation of the amorphous phase to the crystalline or nanocrystalline phase was found in the as-sprayed and the 600 °C annealed coatings during cavitation erosion.

**Keywords** annealing · cavitation erosion · corrosion · Fe-based amorphous coating · high-velocity oxygen-fuel

## Introduction

Hydraulic components, such as impellers, propellers, rudders, and valves, are commonly subjected to the failure caused by cavitation erosion (Ref 1-3). The fluid with high velocity can create a low-pressure zone on the surface of the hydraulic component, resulting in the formation of vapour-filled cavitation bubbles. These bubbles can implode and give off micro-jets and/or shock waves with intense energy, applying repeated load on the surface of the component. As a result, the surface can undergo plastic deformation and will be eroded (Ref 4, 5). Apart from cavitation erosion, the hydraulic components are also exposed to corrosion if operating in a corrosive environment. Meanwhile, since cavitation erosion can enhance chemical reactions (Ref 6), hydraulic components can be susceptible to corrosion during cavitation erosion (Ref 7, 8). In general, cavitation erosion and cavitation erosion-corrosion are the main concerns for hydraulic components.

Applying protective coatings, such as WC-based coatings (Ref 9-11), high-entropy alloy coatings (Ref 12-14), and polyurethane-based coatings (Ref 15-17), is an effective method to address the concerns. Besides the coatings mentioned, thermal-sprayed Fe-based amorphous coatings have shown great potential in resisting cavitation erosion and corrosion in an aggressive environment due to their good mechanical properties and corrosion resistance by the amorphous phases (Ref 18-20). In non-corrosive environments, the Fe-based amorphous coatings prepared by high-velocity oxygen-fuel (HVOF) spraying and high-velocity arc spraying exhibit the cavitation erosion resistance that is

---

Jiewen Wang and Rui Yang have contributed equally to this work.

- ✉ Hua Li  
lihua@nimte.ac.cn
- ✉ Xiuyong Chen  
chenxiuyong@nimte.ac.cn

- <sup>1</sup> Henan Institute of Advanced Technology, Zhengzhou University, Zhengzhou 450003, China
- <sup>2</sup> Zhejiang-Japan Joint Laboratory for Antibacterial and Antifouling Technology, Zhejiang Engineering Research Center for Biomedical Materials, Cixi Institute of Biomedical Engineering, Ningbo Institute of Materials Technology and Engineering, Chinese Academy of Sciences, Ningbo 315201, China

superior to the 13Cr5Ni and the 18Cr9Ni stainless steels (Ref 21, 22). In corrosive environments, the HVOF-sprayed and the arc-sprayed Fe-based amorphous coatings also have good resistance to cavitation erosion which outperforms WC-based coatings (Ref 23–25).

Previous studies also investigated the failure mechanisms of the Fe-based amorphous coatings during cavitation erosion, suggesting that cavitation erosion tends to initiate at the edges of the pores and the interfaces of the splats (Ref 21, 22). Meanwhile, the corrosion resistance of the Fe-based amorphous coatings is also negatively correlated to the porosity (Ref 26, 27). Therefore, it is anticipated that reducing the porosity and improving the adhesion strength at the inter-splat boundaries of Fe-based amorphous coatings can further enhance the resistance to cavitation erosion and erosion-corrosion. Furthermore, the addition of Al<sub>2</sub>O<sub>3</sub> particles can significantly improve the corrosion, wear, and tribo-corrosion behaviours of Fe-based amorphous composite coatings (Ref 28–31). Meanwhile, the dispersion of Al<sub>2</sub>O<sub>3</sub> could also enhance the impact resistance of Fe-based amorphous coating (Ref 32). However, the effect of Al<sub>2</sub>O<sub>3</sub> dispersion on cavitation erosion resistance is barely studied.

In this work, Fe-based amorphous composite coatings reinforced by Al<sub>2</sub>O<sub>3</sub> particles were prepared by HVOF spraying. The as-sprayed coatings were annealed at 600 or 850 °C in a vacuum for 1 h, in an attempt to improve the coating quality and achieve enhanced resistance to cavitation erosion and erosion-corrosion. The work aims to study the effect of annealing on the cavitation erosion resistance of HVOF-sprayed Fe-based amorphous composite coatings in corrosive and non-corrosive environments. The mechanical properties and corrosion resistance of the coatings before and after the annealing were also evaluated. In addition, the microstructural change of the coatings at the early stages of cavitation erosion was also investigated.

## Experimental Procedure

### Materials and Process

HVOF spraying (UniCoatPro-LF, Oerlikon Metco, Switzerland) was used to deposit the Fe-based amorphous composite coating onto the top surface of 316L stainless steel substrates. The feedstock Fe-based composite powder (XY-26F-FJ, Shenyang institute of rare metals Ltd., China) was composed of 75 wt.% Fe-based alloy powder and 25 wt.% Al<sub>2</sub>O<sub>3</sub> powder. The size distribution of the Fe-based alloy powder and the Al<sub>2</sub>O<sub>3</sub> powder ranged from 15 to 45 μm. The SEM images of the feedstock are shown in Fig. 1, and the composition of the Fe-based alloy particles

is tabulated in Table 1. The substrate material was 316L stainless steel (Zechanglong Ltd., China) and was machined into cylinders with a diameter of 20 mm and a thickness of 10 mm.

Before the spraying, the substrates were blasted by 24-grit alumina with 0.3–1.0 MPa compressed air for 1 min. The surface roughness of these grit-blasted substrates was  $1.9 \pm 0.2 \mu\text{m}$  measured by a profilometer (Up-Lambda 2, Rtec Instruments, USA). Then, the grit-blasted substrates were cleaned with acetone to improve adhesion. The parameters for the HVOF spraying process suggested by the powder vendor are tabulated in Table 2. The as-sprayed coatings were annealed at either 600 or 850 °C for 1 h in a vacuum furnace (SQFL-1700, Shanghai Jvjing Precision Instrument Manufacturing Ltd.) at about 100 Pa, then cooled with the furnace, and finally taken out after 12 h. All the samples were ground and polished (finished by 0.05 μm diamond suspension) prior to any characterisations and tests. The artificial seawater (AS) used in this work was prepared as per ASTM D1141-98(2013) (Ref 33).

### Microstructure Characterisations of the Coatings

The as-sprayed and the annealed coatings with polished surfaces or cross-sections were characterised by a scanning electron microscope (SEM, Regulus-8230, Hitachi, Japan) equipped with an energy dispersive x-ray detector (EDX, XFlash 6-100, Bruker, Germany). The porosity was measured from five cross-sectional SEM images at a magnification of 500× by ImageJ software for each coating. The chemical composition of the coatings was characterised by x-ray diffraction (XRD, D8 Advance, Bruker, Germany) with a copper anode at 40 kV and 40 mA scanning at 0.1°/s in a range of 20°–90°. The XRD data were analysed by JADE based on the powder diffraction file database in the software. The degree of non-crystallinity is calculated according to Eq 1, where  $X_a$  is degree of non-crystallinity,  $I_a$  is amorphous scattering intensity, and  $I_c$  is crystal diffraction intensity.

$$X_a = \left( 1 - \frac{I_c}{I_c + I_a} \right) \times 100\% \quad (\text{Eq 1})$$

### Microhardness and Fracture Toughness

The microhardness and fracture toughness tests were conducted on the polished cross-section of the coatings. For the microhardness test, ten random locations at the middle of the coating were indented under a load of 0.2 kgf, and the mean value of the result from each indented site was calculated. The fracture toughness test was performed in

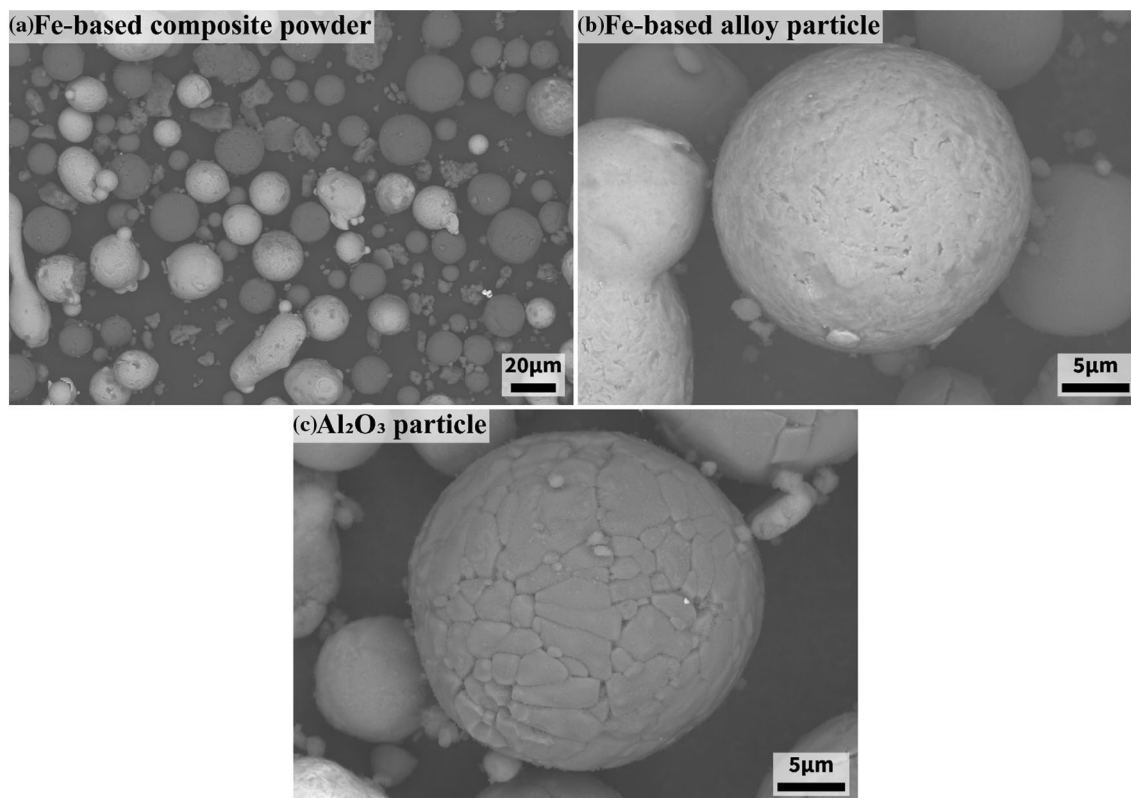


**Fig. 1** SEM images of the feedstock

**Table 1** Elemental composition of the Fe-based alloy particles

Elements	Fe	Cr	Co	Ni	Mo	Si
wt.%	Bal	13.5	8.5	8.0	2.0	0.5

Nominal composition

**Table 2** Parameters employed in the HVOF spraying process

Nitrogen flow, NLPM	5
Oxygen flow, NLPM	600
Kerosene flow, l/h	16
Standoff distance, mm	300
Feed rate, g/min	100
Traverse velocity, mm/s	500
Space between adjacent spraying traces, mm	5
Repetition	10

the same procedure of the microhardness test, but the indentation load was 2.0 kgf. Then, the fracture toughness of the coatings was expressed by the crack extension energy ( $G_C$ , in  $J/m^2$ ) developed by Ostojic et al. (Ref 34). The crack extension was commonly used to evaluate the

fracture toughness of the thermal-sprayed coatings (Ref 35–37). The equation for  $G_C$  is in Eq 2, where  $P$  is the indentation load,  $a$  is the impression half diagonal, and  $c$  is the half of the total length of the major crack.

$$G_C = 6.115 \times 10^{-4} (P a^2 / c^3) \quad (\text{Eq 2})$$

### Electrochemical Test

The corrosion resistance of the polished coatings was evaluated in an electrochemical workstation (CHI-660E, Shanghai Chenhua Instrument Ltd., China) with a three-electrode system, which consisted of the coated sample to be tested, a saturated calomel electrode as the reference, and a platinum plate as the counter electrode. Before the test, the sample was immersed in AS for 2 h, and then the open circuit potential (OCP) of the sample was monitored for 2 min to check whether the OCP of the sample was stabilised. The test was conducted in AS at  $25 \pm 1$  °C. The peak-to-peak amplitude for the electrochemical impedance spectroscopy was 20 mV, and the frequency range was  $10^{-2}$ – $10^5$  kHz where 13 points were sampled per frequency decade. The scan rate for the potentiodynamic polarisation was 10 mV/s, according to other studies on the corrosion behaviour of Fe-based amorphous coatings (Ref 38, 39).

For each coating, the test was repeated three times to check the repeatability.

### Cavitation Erosion Test

The cavitation erosion resistance of the as-sprayed and the annealed coatings with polished surfaces was evaluated as per a modified version of ASTM G32-16(2021)e1 (Ref 40), and the apparatus is shown in Fig. 2. During the cavitation erosion test, the sample was placed on the sample holder, and the top surface of the sample was 1 mm to the sonotrode tip. The rest of the parameters were in accordance with ASTM G32, where the output power was 2 kW, the output frequency was 20 kHz, the peak-to-peak amplitude was 50  $\mu\text{m}$ , and the test solution was kept at  $25 \pm 1$  °C. The samples were tested either in deionised water (DW) or AS. At each test interval of 1 h, the sample was weighed to check its mass loss. The eroded surface and cross-section of the coatings after the 10-h cavitation erosion test in both DW and AS were characterised by SEM. In addition, the behaviour of the  $\text{Al}_2\text{O}_3$  particles in the as-sprayed coating exposed to cavitation erosion in AS was also investigated by SEM. Furthermore, the eroded coatings at the early stage of cavitation erosion were examined by XRD using the same parameters mentioned before.

## Results and Discussion

### Microstructure of the Coatings

The SEM images of the surface and the cross-section of the coatings are shown in Fig. 3(a1)-(c3). The dark regions in the SEM images were  $\text{Al}_2\text{O}_3$  particles (Fig. 3a3-c3) confirmed by the EDX results (Fig. 3a4-c5), and the content of  $\text{Al}_2\text{O}_3$  in the as-sprayed coating was  $1.4 \pm 0.2$  wt.%. Meanwhile, inter-splat boundaries were found in all the coatings (Fig. 3a3-c3). However, the space at the inter-splat boundaries of the 850 °C annealed coating was

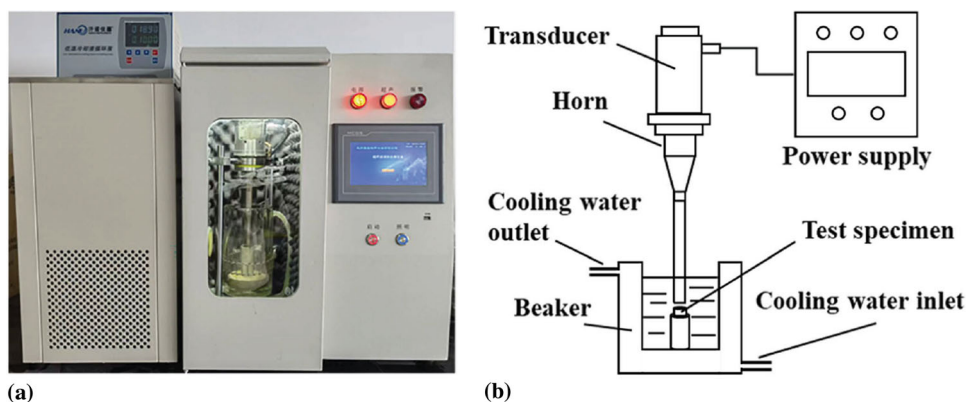
reduced, and the inter-splat boundaries were barely identified (Fig. 3c3), suggesting the improved adhesion at the inter-splat boundaries of the 850 °C annealed coating. The porosity of the as-sprayed, the 600 °C annealed, and the 850 °C annealed coatings was  $1.6 \pm 0.3$ ,  $1.4 \pm 0.4$ , and  $0.3 \pm 0.2\%$ , respectively. The reduced space at the inter-splat boundaries and the large decrease in porosity of the 850 °C annealed coating indicated that the annealing at 850 °C could effectively densify the HVOF-sprayed Fe-based amorphous composite coating. The densification of Fe-based amorphous coatings by heat-treatment was also reported by other studies (Ref 36, 41, 42) and could be attributed to the self-fluxing reaction in the Fe-based alloy during the heat treatment (Ref 36). In addition, the precipitation and growth of some other phases (Fig. 4) during the heat treatment may also affect the porosity of the coating.

The XRD spectra of the coatings are presented in Fig. 4 with the main peaks marked. The spectrum of the as-sprayed coating showed a broad halo at the scattering angle ( $2\theta$ ) of  $40^\circ$ - $50^\circ$ , indicating the coating exhibited amorphous phases. However, some crystalline peaks, such as the peaks of  $\alpha$ -Fe and  $\text{Al}_2\text{O}_3$ , were also identified, suggesting that the as-sprayed coating was not fully amorphous. After the annealing at 600 °C, the halo was narrowed, and the intensity of the peak of  $\alpha$ -Fe increased, indicating a reduced portion of the amorphous phase. The annealing at 850 °C resulted in a significant increase in the  $\alpha$ -Fe peak and the absence of the halo, indicating the coating was mostly crystalline. The degree of non-crystallinity of the as-sprayed, the 600 °C annealed, and the 850 °C annealed coatings was 79.9, 59.6, and 35.5%, respectively.

### Mechanical Properties

The microhardness of the coatings is shown in Fig. 5(a). All the coatings exhibited the microhardness that was much higher than the 316L stainless steel substrates ( $172 \pm 5$   $\text{Hv}_{0.2}$ ). However, the annealing could result in a decrease in

**Fig. 2** The apparatus for cavitation erosion test: (a) photo, and (b) schematic diagram



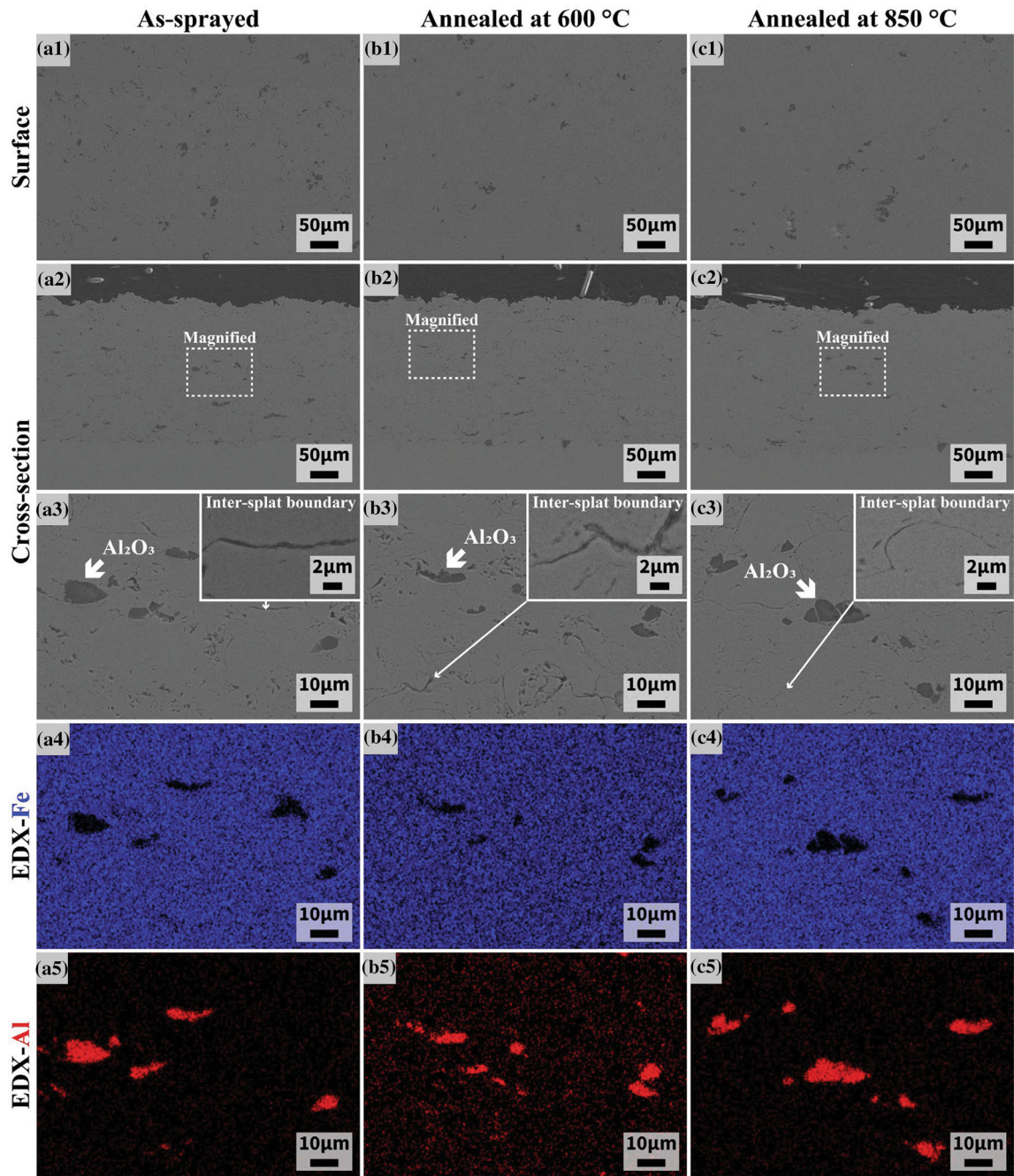


**Fig. 3** SEM and EDX results of the coatings

microhardness. For the coating annealed at 850 °C, the microhardness decreased significantly from  $880 \pm 17$  to  $652 \pm 16$  Hv<sub>0.2</sub>. Such a great reduction in microhardness was possibly attributed to the decrease in the content of the hard amorphous phase after the annealing (Fig. 4). Nevertheless, the fracture toughness of the annealed coatings was enhanced according to Fig. 5(b). The 850 °C annealed coating exhibited a significant enhancement in the crack extension energy, which was about 2.4 times that of the as-sprayed coating. The reduced porosity of the annealed

coatings may contribute to the improved fracture toughness. Furthermore, the increased fracture toughness also indicates the improved adhesion at the inter-splat boundaries of the coatings after the annealing.

### Electrochemical Test

The electrochemical test results are presented in Fig. 6 and Table 3. The Nyquist plots in Fig. 6(a) showed that the semicircle radius of the annealed coatings was smaller than

that of the as-sprayed coatings, suggesting that the annealing could compromise the corrosion resistance of the HVOF-sprayed Fe-based amorphous composite coating. An equivalent circuit model based on the electrochemical impedance spectroscopy results is presented in Fig. 6(a). The polarization resistance ( $R_p$ ) is used to evaluate the corrosion resistance, which is the sum of the corrosion product film resistance ( $R_c$ ) and the charge transfer resistance ( $R_{ct}$ ). A low  $R_p$  value means corrosion is likely to occur (Ref 43). Therefore, the  $R_p$  values in Table 3 also suggested that the corrosion resistance of the annealed coatings was inferior to the as-sprayed coating. The Tafel curves of the coatings are presented in Fig. 6(b), and the corresponding fitting results are tabulated in Table 3, which are the corrosion potential ( $E_{corr}$ ) and the corrosion current density ( $I_{corr}$ ).  $E_{corr}$  is positively correlated to corrosion resistance, while  $I_{corr}$  is negatively correlated (Ref 44). Hence, the results again indicated that the annealing could negatively affect the corrosion resistance of the coatings.

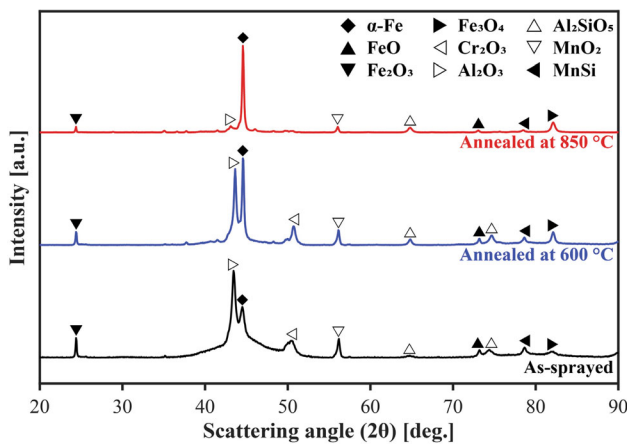


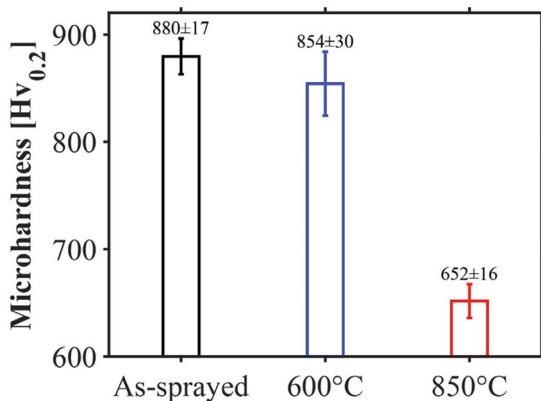
Fig. 4 XRD spectra of the coatings

The compromised corrosion resistance of the annealed coatings was attributed to the crystallisation during the annealing. The increased content of the crystalline phases resulted in the increased grain boundaries, which provided more sites for the preferential attack of corrosion (Ref 42, 45, 46). Furthermore, other studies also found that the passive films formed in amorphous materials were different from those in crystalline materials. Specifically, the corrosion resistance of Fe-based amorphous coatings was negatively correlated to the amount of the crystalline phases due to the heterogeneity of the passive films by the formation of the carbides by the annealing (Ref 47). Meanwhile, the passive film formed in crystalline materials exhibited more defects and was less compact than that formed in amorphous materials (Ref 48). Therefore, both annealed coatings in this work were less corrosion-resistant than the as-sprayed coating. In addition, it is worth mentioning that the corrosion resistance of the 850 °C annealed coating was superior to that of the 600 °C annealed coating (Fig. 6 and Table 3) because of the extremely low porosity of the 850 °C annealed coating since a compacted structure is beneficial to resisting corrosion (Ref 26, 27, 49).

**Cavitation Erosion**

The cumulative erosion and the erosion rate of the coatings during the cavitation erosion test in DW and AS are presented in Fig. 7, and the SEM characterisation of the eroded coatings after the 10 h test is shown in Figs. 8 and 9. Generally, the erosion of the coatings in the non-corrosive environment was less severe than that in the corrosive environment. In DW, the 850 °C annealed coating exhibited the lowest erosion and erosion rate, while the as-sprayed coating had the greatest (Fig. 7a, c). The SEM images also showed that the erosion crater in the 850 °C

**(a) Microhardness**



**(b) Fracture toughness**

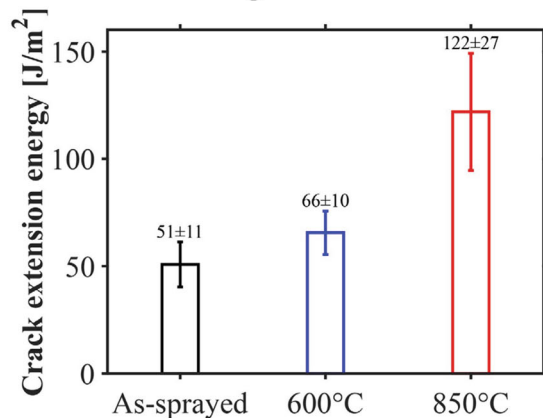
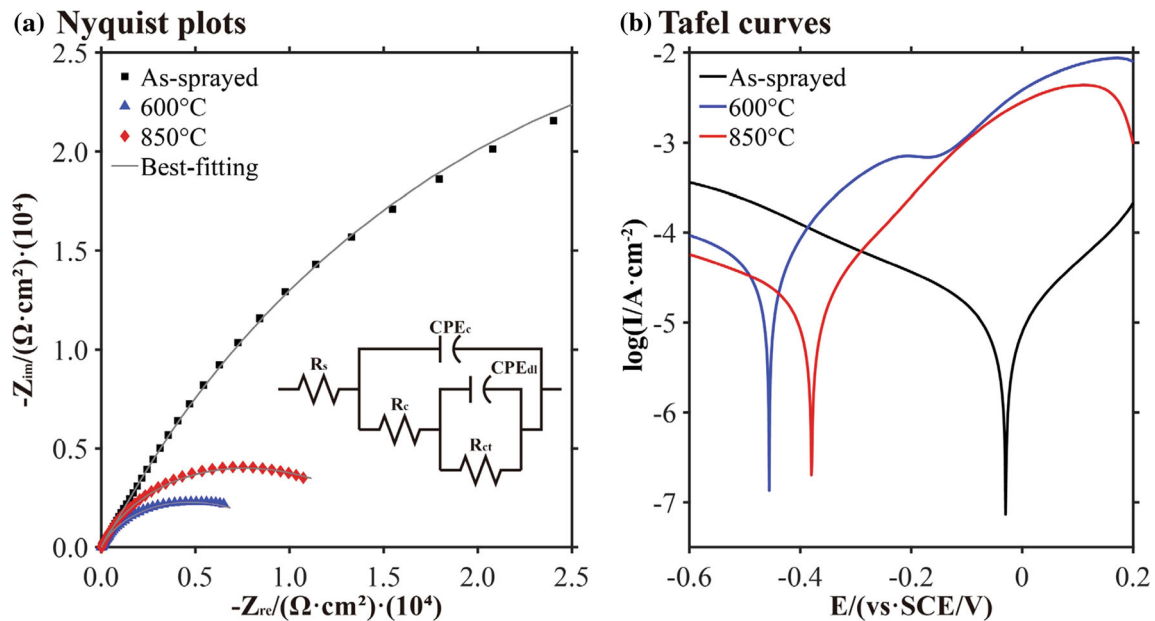


Fig. 5 Mechanical properties of the coatings. (a) Microhardness measured at 0.2 kgf; (b) Fracture toughness in terms of crack extension energy measured at 2.0 kgf



**Fig. 6** Electrochemical properties of the coatings. (a) Nyquist plots and equivalent circuit model, where  $R_s$ ,  $R_c$ ,  $R_{ct}$ ,  $CPE_c$ , and  $CPE_{dl}$ , are related to the solution resistance, corrosion product film resistance,

charge transfer resistance, coating capacitance and double layer capacitance, respectively; (b) Tafel curves

**Table 3** Electrochemical parameters of the coatings

Coatings	$R_p$ , $\Omega \text{ cm}^2$	$E_{\text{corr}}$ , V	$I_{\text{corr}}$ , $\text{A cm}^{-2}$
As-sprayed	$8.57 \times 10^4$	-0.030	$9.89 \times 10^{-6}$
600 °C annealed	$1.08 \times 10^4$	-0.456	$4.53 \times 10^{-5}$
850 °C annealed	$1.78 \times 10^4$	-0.380	$1.80 \times 10^{-5}$

$R_p$ ,  $E_{\text{corr}}$ , and  $I_{\text{corr}}$  are the polarization resistance, corrosion potential, and corrosion current, respectively

annealed coating was much smaller than that in the as-sprayed coating (Fig. 8a3-c3). In AS, the 850 °C annealed coating still exhibited the lowest erosion and erosion rate, but the 600 °C annealed coating had the greatest mass loss (Fig. 7b, d). The SEM images also showed that the as-sprayed and the 850 °C annealed coatings had the craters with similar sizes, while the crater in the 600 °C annealed coating was the largest (Fig. 9a3-c3). In addition, some unmelted and partially melted particles were exposed and could be observed from the as-sprayed and the 600 °C annealed coatings (Figs. 8a1-b2 and 9 a1-b2) during cavitation erosion. Meanwhile, it seemed that the erosion preferentially occurred near these particles, possibly attributed to the poor adhesion. On the other hand, unmelted and partially melted particles were barely observed from the 850 °C annealed coatings (Figs. 8c and 9c). This indicates that the adhesion at the inter-splat boundaries around the unmelted and partially melted particles was improved, and thus these particles were not

exposed easily during cavitation erosion. According to the results above, the 850 °C annealed coating had the best cavitation erosion resistance in both solutions, while the as-sprayed coating and the 600 °C annealed coating were the least resistant to cavitation erosion in DW and AS, respectively.

The behaviour of the  $\text{Al}_2\text{O}_3$  particles in the as-sprayed coating during the cavitation erosion test was also investigated by taking a series of SEM images at the same site at different test intervals (Fig. 10). The results showed that the  $\text{Al}_2\text{O}_3$  particles were easily detached from the coating surface at the early stage of cavitation erosion, leaving some rough pits on the surface (Fig. 10a, b), which was possibly attributed to the weak adhesion at the phase boundaries. Then, these pits expanded quickly and became a large crater when the coating was subjected to cavitation erosion further, resulting in severe erosion (Fig. 10c). The SEM observation on the behaviour of the  $\text{Al}_2\text{O}_3$  particles in the coating during cavitation erosion suggested that the addition of  $\text{Al}_2\text{O}_3$  to the Fe-based amorphous composite coating may compromise the cavitation erosion resistance of the coating. The addition of  $\text{Al}_2\text{O}_3$  particles was supposed to improve the impact resistance of the coating (Ref 32), but the cavitation erosion resistance of the coating was decreased. This is because the improved impact resistance is in macro scale. Nevertheless, the impact by cavitation bubble implosion applies an intense load in a small area, which is micron scale (about several microns). When the impact was at the phase boundaries of the  $\text{Al}_2\text{O}_3$  and the

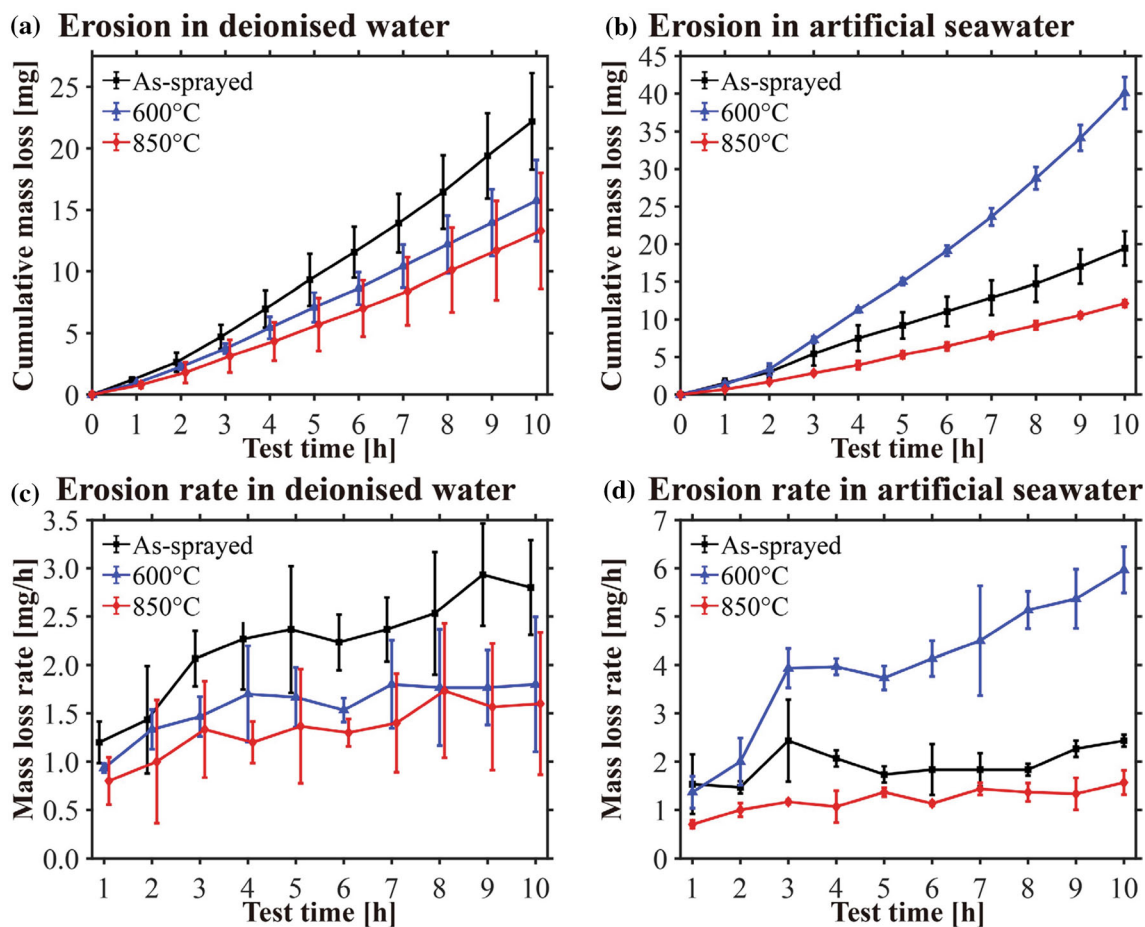


**Fig. 7** Cavitation erosion performance of the coatings

metallic phases, Al<sub>2</sub>O<sub>3</sub> particles would detach from the metal matrix easily.

Literature reported that some materials exposed to cavitation erosion could undergo stress-induced phase transformation, which allowed the materials having good cavitation erosion resistance (Ref 50, 51). Moreover, the amorphous phase in the Fe-based coatings could transform into crystalline phases during cavitation erosion (Ref 52). Thus, it is worthwhile to examine the eroded coatings in this work by XRD. According to the results (Fig. 11), the test solutions, DW or AS, could not affect the XRD spectra for each coating exposed to cavitation erosion for the same duration. Nevertheless, the spectra of the as-sprayed and the 600 °C annealed coatings changed after cavitation erosion (Fig. 11a-d). For both coatings, the relative intensity of the  $\alpha$ -Fe peak grew as the extension of the exposure to cavitation erosion (Fig. 11a-d). Meanwhile, the degree of non-crystallinity of the as-sprayed and the 600 °C annealed coatings decreased from 79.9 to 68.0% and 59.6 to 51.5%, respectively, after cavitation erosion for 2 h. The increased relative intensity of the  $\alpha$ -Fe peak and the decreased degree of non-crystallinity indicated that a

portion of the amorphous phase transformed into crystalline or nanocrystalline phases in the as-sprayed and the 600 °C annealed coatings during cavitation erosion. In addition, the detachment of the Al<sub>2</sub>O<sub>3</sub> particles (Fig. 10) may also contribute to the increase in the relative intensity of the  $\alpha$ -Fe peak. However, for the 850 °C annealed coating, there was almost no difference in the XRD spectra before and after cavitation erosion (Fig. 11e, f), and the change in the degree of non-crystallinity was negligible. Furthermore, it is worth mentioning that the scattering angle of the  $\alpha$ -Fe did not change after cavitation erosion, meaning that there was barely stress accumulation in the coatings during cavitation erosion. Hence, the impact energy by cavitation was consumed by phase transformation, plastic deformation, and erosion.

Although the as-sprayed and the 600 °C annealed coatings could undergo stress-induced phase transformation during cavitation erosion (Fig. 11a-d), their cavitation erosion resistance was inferior to that of the 850 °C annealed coating (Fig. 7). In DW (Fig. 7a, c), the cavitation erosion resistance of the coatings was positively correlated to the fracture toughness (Fig. 5b) and negatively



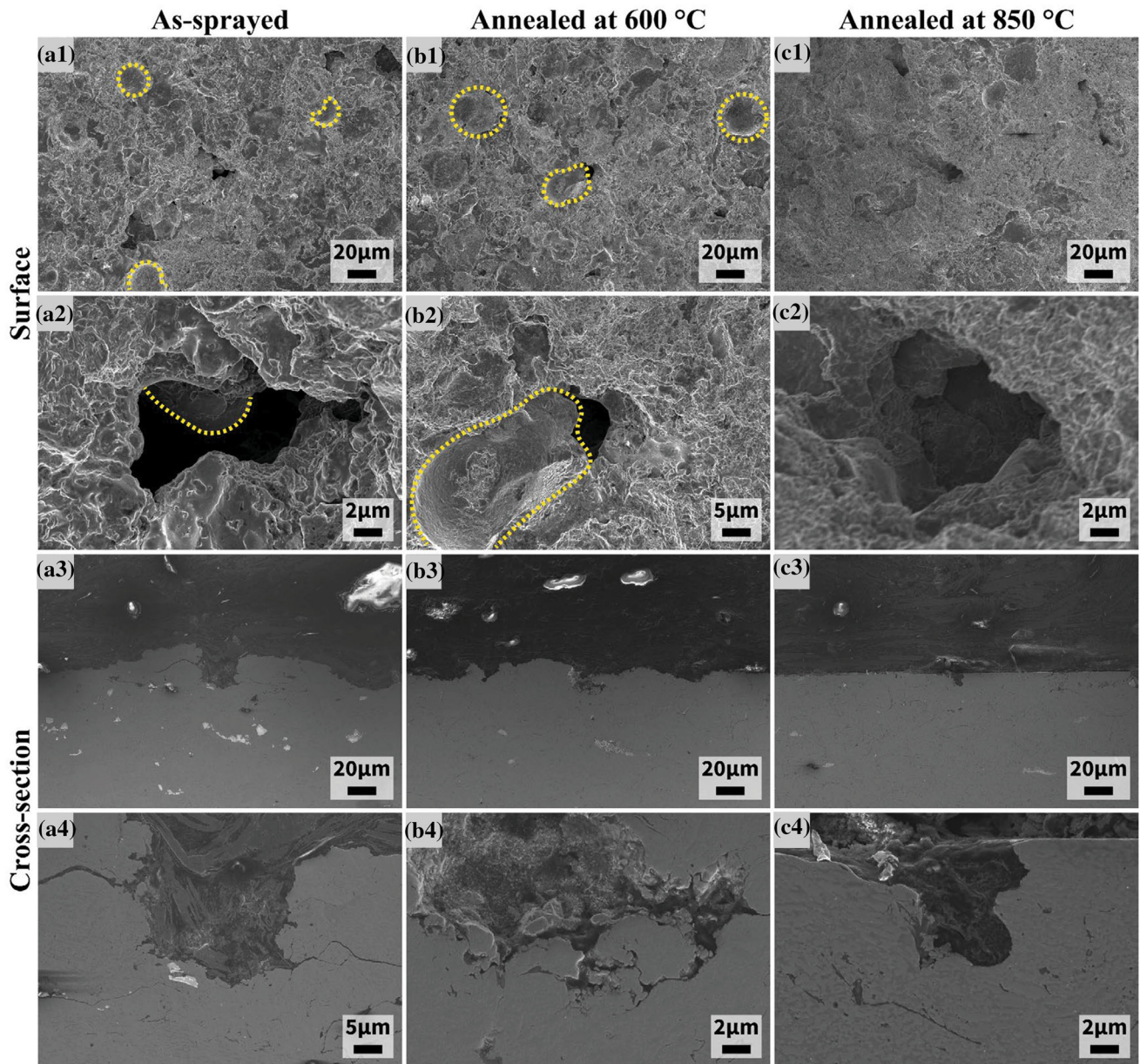


**Fig. 8** SEM images of the samples after cavitation erosion for 10 h in DW. 1-2, SEM images of the eroded surface at low and high magnifications, where the dotted lines highlight the exposed unmelted

and partially melted particles; 3-4, SEM images of the cross-section of the eroded coatings at low and high magnifications

correlated to the porosity. Such correlations are common in other coatings subjected to cavitation erosion. High fracture toughness means good adhesion at the inter-splat boundaries, and thus the coating with high fracture toughness can effectively absorb the cavitation impact energy and inhibit the formation and propagation of microcracks during cavitation erosion (Ref 9, 53, 54). Pores are generally considered the potential sites for crack nucleation and are preferentially damaged during cavitation erosion (Ref 9, 55, 56). Therefore, the enhancement of the cavitation erosion resistance of the coatings could be

achieved by the improvement of the fracture toughness and the reduction in the porosity via annealing. However, the decrease in the hardness (Fig. 5a) did not have any negative effect on the cavitation erosion resistance, though high hardness is believed to be beneficial to achieving good cavitation erosion resistance (Ref 57), suggesting cavitation erosion resistance is predominant by fracture toughness and porosity instead of hardness solely.

For the coatings subjected to cavitation erosion in AS, the 850 °C annealed coating still exhibited the lowest loss (Fig. 7b, d) despite the decreased corrosion resistance

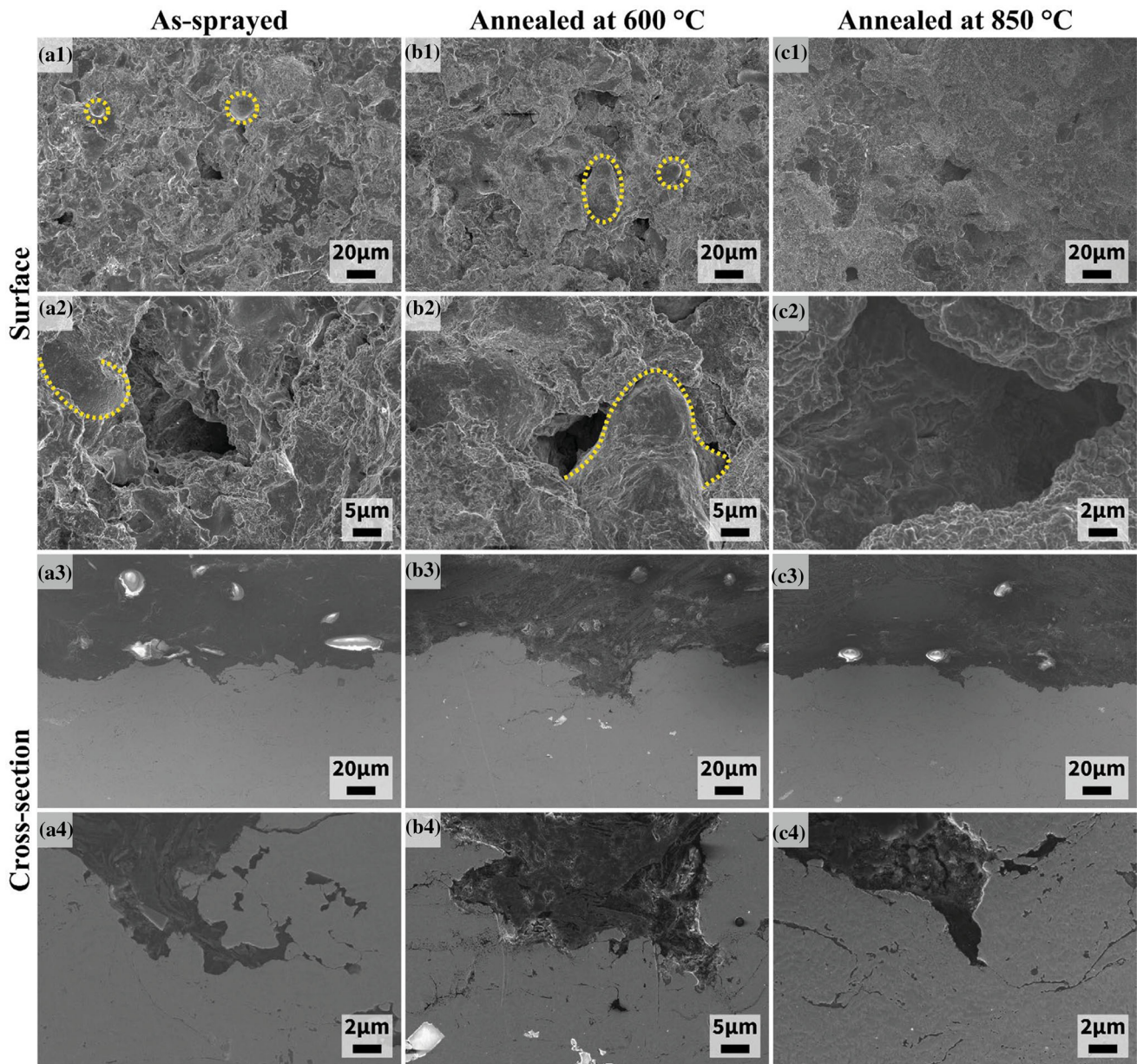


**Fig. 9** SEM images of the samples after cavitation erosion for 10 h in AS. 1-2, SEM images of the eroded surface at low and high magnifications, where the dotted lines highlight the exposed unmelted

and partially melted particles; 3-4, SEM images of the cross-section of the eroded coatings at low and high magnifications

(Fig. 6 and Table 3), indicating that the material damage was mainly caused by cavitation erosion. Nevertheless, the erosion of the coatings in AS was more severe than that in DW (Fig. 7), indicating that the effect of corrosion was also significant for the coatings subjected to cavitation erosion in corrosive environments. Hence, the loss of the as-sprayed coating was lower than that of the 600 °C annealed coating when exposed to cavitation erosion in AS (Fig. 7b, d) because the former had the best corrosion resistance while the latter had the worst (Fig. 6 and Table 3). Meanwhile, the best cavitation erosion resistance

of the 850 °C annealed coating in AS could be attributed to the good fracture toughness (Fig. 5b) and low porosity by the annealing without much decrease in the corrosion resistance (Fig. 6 and Table 3). Therefore, the results presented in this work prove that a specific annealing process can enhance the cavitation erosion (and erosion-corrosion) resistance of HVOF-sprayed Fe-based amorphous coatings by improving fracture toughness and reducing porosity. For future work, it is worthwhile to develop a post-treatment approach to achieving good fracture toughness and low porosity of HVOF-sprayed Fe-

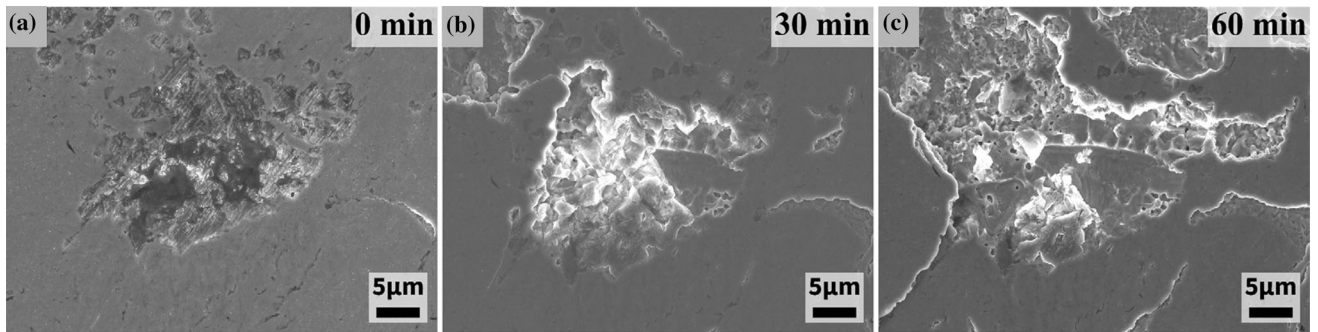


**Fig. 10** SEM images of the  $\text{Al}_2\text{O}_3$  particles in the as-sprayed coating exposed to cavitation erosion in AS for 0, 30, and 60 min. Images were taken at the same site

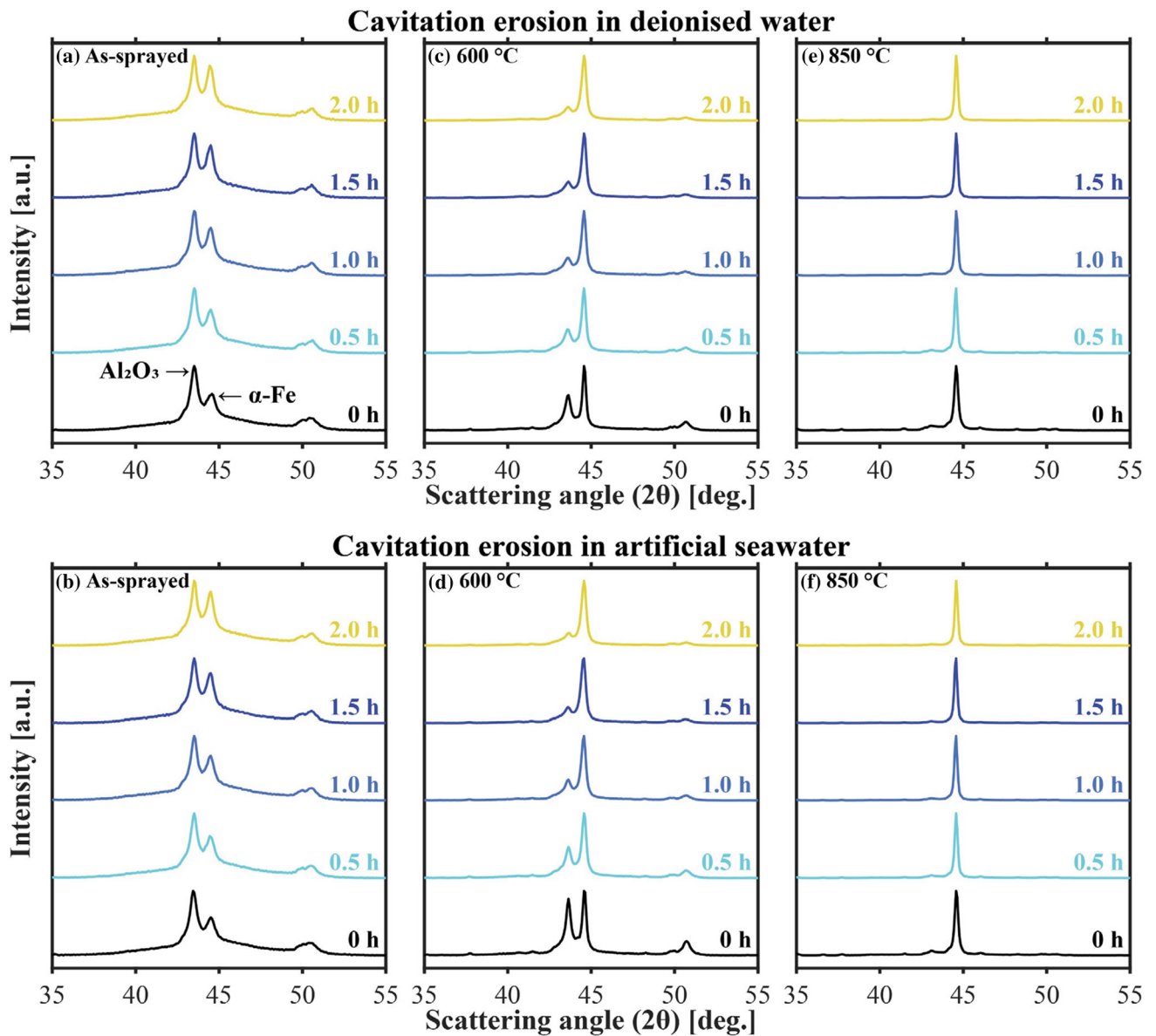


**Fig. 11** XRD spectra of the coatings after the exposure to cavitation erosion in DW and AS for 0, 0.5, 1.0, 1.5, and 2.0 h

based amorphous coatings with a minimal crystalline phase transformation.

## Conclusion

HVOF-sprayed post-annealed Fe-based amorphous composite coatings were prepared in this work, whose microstructures, mechanical properties, and corrosion resistance were investigated. The cavitation erosion resistance of the coatings in DW and AS was evaluated. According to the results, the following findings were concluded:

- The annealing improved the fracture toughness and reduced the porosity of the coatings.
- However, the amorphous phase was transformed to crystalline or nanocrystalline phases during the annealing, which compromised the hardness and corrosion resistance of the coatings.
- The 850 °C annealed coating exhibited the best cavitation erosion resistance in DW and in AS because of its best fracture toughness, lowest porosity, and limited reduction in corrosion resistance.
- The Al<sub>2</sub>O<sub>3</sub> particles for the reinforcement were preferentially eroded during cavitation erosion and may compromise the cavitation erosion resistance of the Fe-based amorphous coating.
- Stress-induced crystallisation of the amorphous phase was found in the as-sprayed and the 600 °C annealed coatings during cavitation erosion.

**Acknowledgment** This research was funded by the Zhejiang Provincial Natural Science Foundation of China (Grant # LZ22E090001), and Ningbo 3315 Talents Program (Grant # 2020A-29-G).

## References

1. X. Liu, Y.Y. Luo, and Z.W. Wang, A Review on Fatigue Damage Mechanism in Hydro Turbines, *Renew. Sust. Energ. Rev.*, 2016, **54**, p 1-14. <https://doi.org/10.1016/j.rser.2015.09.025>
2. B.K. Sreedhar, S.K. Albert, and A.B. Pandit, Cavitation Damage: Theory and Measurements: A Review, *Wear*, 2017, **372**, p 177-196. <https://doi.org/10.1016/j.wear.2016.12.009>
3. R.E. Bensow, Numerical Prediction of Cavitation and Related Nuisances in Marine Propulsion Systems, *Cavitation and Bubble Dynamics*. P. Koukouvinis, M. Gavaises Ed., Elsevier, 2021, p 111-132
4. C.E. Brennen, Cavitation Bubble Collapse, *Cavitation and Bubble Dynamics*. C.E. Brennen Ed., Cambridge University Press, 2013, p 59-88
5. G.L. Chahine, J.P. Franc, and A. Karimi, Cavitation and Cavitation Erosion, *Advanced Experimental and Numerical Techniques for Cavitation Erosion Prediction*. K.H. Kim, G. Chahine, J.P. Franc, A. Karimi Ed., Springer Netherlands, Dordrecht, 2014, p 3-20
6. T.J. Mason and J.P. Lorimer, *Sonoelectrochemistry, Applied Sonochemistry: Uses of Power Ultrasound in Chemistry and Processing*, Wiley, 2002, p 225-266
7. C.T. Kwok, F.T. Cheng, and H.C. Man, Synergistic Effect of Cavitation Erosion and Corrosion of Various Engineering Alloys in 3.5% NaCl Solution, *Mater. Sci. Eng. A*, 2000, **290**(1-2), p 145-154. [https://doi.org/10.1016/s0921-5093\(00\)00899-6](https://doi.org/10.1016/s0921-5093(00)00899-6)
8. J. Ryl, K. Darowicki, and P. Slepiski, Evaluation of Cavitation Erosion-Corrosion Degradation of Mild Steel by Means of Dynamic Impedance Spectroscopy in Galvanostatic Mode, *Corros. Sci.*, 2011, **53**(5), p 1873-1879. <https://doi.org/10.1016/j.corsci.2011.02.004>
9. J. Liu, T. Chen, C. Yuan, and X. Bai, Performance Analysis of Cavitation Erosion Resistance and Corrosion Behavior of HVOF-Sprayed WC-10Co-4Cr, WC-12Co, and Cr<sub>3</sub>C<sub>2</sub>-NiCr Coatings, *J. Therm. Spray Technol.*, 2020, **29**(4), p 798-810. <https://doi.org/10.1007/s11666-020-00994-y>
10. Y. Korobov, H. Alwan, N. Soboleva, A. Makarov, N. Lezhnin, V. Shumyakov, M. Antonov, and M. Deviatiarov, Cavitation Resistance of WC-10Co4Cr and WC-20CrC-7Ni HVOF Coatings, *J. Therm. Spray Technol.*, 2022, **31**(1-2), p 234-246. <https://doi.org/10.1007/s11666-021-01242-7>
11. R. Yang, N. Huang, Y. Tian, J. Qin, P. Lu, H. Chen, H. Li, and X. Chen, Insights into the Exceptional Cavitation Erosion Resistance of Laser Surface Melted Ni-WC Composites: The Effects of WC Morphology and Distribution, *Surf. Coat. Technol.*, 2022, **444**, p 128685. <https://doi.org/10.1016/j.surfcoat.2022.128685>
12. S. Zhang, C.L. Wu, C.H. Zhang, M. Guan, and J.Z. Tan, Laser Surface Alloying of FeCoCrAlNi High-Entropy Alloy on 304 Stainless Steel to Enhance Corrosion and Cavitation Erosion Resistance, *Opt. Laser Technol.*, 2016, **84**, p 23-31. <https://doi.org/10.1016/j.optlastec.2016.04.011>
13. C.L. Wu, S. Zhang, C.H. Zhang, H. Zhang, and S.Y. Dong, Phase Evolution and Cavitation Erosion-Corrosion Behavior of FeCo-CrAlNiTiX High Entropy Alloy Coatings on 304 Stainless Steel by Laser Surface Alloying, *J. Alloys Compd.*, 2017, **698**, p 761-770. <https://doi.org/10.1016/j.jallcom.2016.12.196>
14. R.B. Nair, H.S. Arora, S. Mukherjee, S. Singh, H. Singh, and H.S. Grewal, Exceptionally High Cavitation Erosion and Corrosion Resistance of a High Entropy Alloy, *Ultrason. Sonochem.*, 2018, **41**, p 252-260. <https://doi.org/10.1016/j.ultsonch.2017.09.044>
15. X.N. Qiao, R.R. Chen, H.S. Zhang, J.Y. Liu, Q. Liu, J. Yu, P.L. Liu, and J. Wang, Outstanding Cavitation Erosion Resistance of Hydrophobic Polydimethylsiloxane-Based Polyurethane Coatings, *J. Appl. Polym. Sci.*, 2019, **136**(25), p 47668. <https://doi.org/10.1002/app.47668>
16. H.C. Yang, M.L. Zhang, R.R. Chen, Q. Liu, J.Y. Liu, J. Yu, H.S. Zhang, P.L. Liu, C.G. Lin, and J. Wang, Polyurethane Coating with Heterogeneity Structure Induced by Microphase Separation: A New Combination of Antifouling and Cavitation Erosion Resistance, *Prog. Org. Coat.*, 2021, **151**, p 106032. <https://doi.org/10.1016/j.porgcoat.2020.106032>
17. N. Li, R. Yang, Y. Tian, P.F. Lu, N.L. Huang, H. Li, and X.Y. Chen, Synthesis of Durable Hydrophobic Fluorinated Polyurethanes with Exceptional Cavitation Erosion Resistance, *Tribol. Int.*, 2023, **177**, p 107973. <https://doi.org/10.1016/j.triboint.2022.107973>
18. W.M. Guo, Y.P. Wu, J.F. Zhang, S. Hong, G.Y. Li, G.B. Ying, J. Guo, and Y.J. Qin, Fabrication and Characterization of Thermal-Sprayed Fe-Based Amorphous/Nanocrystalline Composite Coatings: An Overview, *J. Therm. Spray Technol.*, 2014, **23**(7), p 1157-1180. <https://doi.org/10.1007/s11666-014-0096-z>
19. B. Huang, C. Zhang, G. Zhang, and H.L. Liao, Wear and Corrosion Resistant Performance of Thermal-Sprayed Fe-Based

- Amorphous coatings: A Review, *Surf. Coat. Technol.*, 2019, **377**, p 124896. <https://doi.org/10.1016/j.surfcoat.2019.124896>
20. R.F. Vaz, A.G.M. Pukasiewicz, I.B.A.F. Siqueira, G.B. Sucharski, A. Chicoski, and R. Tristante, Thermal Spraying of FeMnCrSi Alloys: An Overview, *Int. Thermal Spray Conf.*, 2021, **2021**, p 431-439.
  21. Y.P. Wu, P.H. Lin, C.L. Chu, Z.H. Wang, M. Cao, and J.H. Hu, Cavitation Erosion Characteristics of a Fe-Cr-Si-B-Mn Coating Fabricated by High Velocity Oxy-Fuel (HVOF) Thermal Spray, *Mater. Lett.*, 2007, **61**(8-9), p 1867-1872. <https://doi.org/10.1016/j.matlet.2006.07.147>
  22. Z. Wang, X. Zhang, J. Cheng, J. Lin, and Z. Zhou, Cavitation Erosion Resistance of Fe-Based Amorphous/Nanocrystal Coatings Prepared by High-Velocity Arc Spraying, *J. Therm. Spray Technol.*, 2014, **23**(4), p 742-749. <https://doi.org/10.1007/s11666-014-0074-5>
  23. Z.B. Zheng, Y.G. Zheng, W.H. Sun, and J.Q. Wang, Erosion-Corrosion of HVOF-Sprayed Fe-Based Amorphous Metallic Coating Under Impingement by a Sand-Containing NaCl Solution, *Corros. Sci.*, 2013, **76**, p 337-347. <https://doi.org/10.1016/j.corsci.2013.07.006>
  24. S. Hong, Y.P. Wu, J.F. Zhang, Y.G. Zheng, Y. Zheng, and J.R. Lin, Synergistic Effect of Ultrasonic Cavitation Erosion and Corrosion of WC-CoCr and FeCrSiBMn Coatings Prepared by HVOF Spraying, *Ultrason. Sonochem.*, 2016, **31**, p 563-569. <https://doi.org/10.1016/j.ulsonch.2016.02.011>
  25. J.R. Lin, Z.H. Wang, J.B. Cheng, M. Kang, X.Q. Fu, and S. Hong, Evaluation of Cavitation Erosion Resistance of Arc-Sprayed Fe-Based Amorphous/Nanocrystalline Coatings in NaCl Solution, *Results Phys.*, 2019, **12**, p 597-602. <https://doi.org/10.1016/j.rinp.2018.12.007>
  26. Y.J. Kim, J.W. Jang, D.W. Lee, and S. Yi, Porosity Effects of a Fe-Based Amorphous/Nanocrystals Coating Prepared by a Commercial High Velocity Oxy-Fuel Process on Cavitation Erosion Behaviors, *Met. Mater. Int.*, 2015, **21**(4), p 673-677. <https://doi.org/10.1007/s12540-015-4580-x>
  27. M.M. Liu, Z.B. Wang, H.X. Hu, L.M. Zhang, and Y.G. Zheng, Effect of Sealing Treatments on Erosion-Corrosion of a Fe-Based Amorphous Metallic Coating in 3.5 wt.% NaCl Solution with 2 wt.% Sand, *Metals*, 2022, **12**(4), p 680. <https://doi.org/10.3390/met12040680>
  28. Z.H. Chu, S.K. Teng, Y.Y. Zhou, X.W. Zheng, J.X. Xu, F. Wang, and B.S. Zhang, The Corrosion Resistance and Mechanism of AT13/Fe-Based Amorphous Composite Coatings, *Micromachines*, 2022, **13**(1), p 56. <https://doi.org/10.3390/mi13010056>
  29. I.D. Kuchumova, N.Y. Cherkasova, I.S. Batraev, V.S. Shikalov, A.V. Ukhina, G.Y. Koga, and A.M. Jorge, Wear-Resistant Fe-Based Metallic Glass-Al<sub>2</sub>O<sub>3</sub> Composite Coatings Produced by Detonation Spraying, *J. Therm. Spray Technol.*, 2022, **31**(4), p 1355-1365. <https://doi.org/10.1007/s11666-021-01299-4>
  30. M. Yasir, C. Zhang, W. Wang, P. Xu, and L. Liu, Wear Behaviors of Fe-Based Amorphous Composite Coatings Reinforced by Al<sub>2</sub>O<sub>3</sub> Particles in Air and in NaCl Solution, *Mater. Des.*, 2015, **88**, p 207-213. <https://doi.org/10.1016/j.matdes.2015.08.142>
  31. M. Yasir, C. Zhang, W. Wang, Z.W. Zhang, and L. Liu, Tribocorrosion Behavior of Fe-Based Amorphous Composite Coating Reinforced by Al<sub>2</sub>O<sub>3</sub> in 3.5% NaCl Solution, *J. Therm. Spray Technol.*, 2016, **25**(8), p 1554-1560. <https://doi.org/10.1007/s11666-016-0457-x>
  32. M. Yasir, C. Zhang, W. Wang, Y.Z. Jia, and L. Liu, Enhancement of Impact Resistance of Fe-Based Amorphous Coating by Al<sub>2</sub>O<sub>3</sub> Dispersion, *Mater. Lett.*, 2016, **171**, p 112-116. <https://doi.org/10.1016/j.matlet.2016.02.060>
  33. ASTM D1141-98, *Standard Practice for the Preparation of Substitute Ocean Water*, American Society for Testing and Materials International, 2013.
  34. P. Ostojic, and R. Mcpherson, Toughness: Its Characteristics in Thermally Sprayed Coatings, *Mater. Sci. Forum*, 1991, **34-36**, p 451-455.
  35. L. Zhu, J.N. He, D.A.R. Yan, L.S. Xiao, Y.C. Dong, J.X. Zhang, and H.L. Liao, Synthesis and Microstructure Observation of Titanium Carbonitride Nanostructured Coatings Using Reactive Plasma Spraying in Atmosphere, *Appl. Surf. Sci.*, 2011, **257**(20), p 8722-8727. <https://doi.org/10.1016/j.apsusc.2011.05.056>
  36. W.H. Liu, F.S. Shieu, and W.T. Hsiao, Enhancement of Wear and Corrosion Resistance of Iron-Based Hard Coatings Deposited by High-Velocity Oxygen Fuel (HVOF) Thermal Spraying, *Surf. Coat. Technol.*, 2014, **249**, p 24-41. <https://doi.org/10.1016/j.surfcoat.2014.03.041>
  37. Y.F. Qin, Z.H. He, H.J. Zhao, J.S. Song, J.B. Lu, Z.W. Ma, and J.N. He, Study on the Crystallization Behaviors and Mechanical Properties of Reactive Plasma Sprayed TiCN Coatings, *Ceram. Int.*, 2022, **48**(20), p 30490-30498. <https://doi.org/10.1016/j.ceramint.2022.06.329>
  38. S. Cui, H.M. Zhai, W.S. Li, X.J. Fan, X.Q. Li, W.C. Ning, and D.S. Xiong, Microstructure and Corrosion Resistance of Fe-Based Amorphous Coating Prepared by Detonation Spray, *Surf. Coat. Technol.*, 2020, **399**(10), p 126096. <https://doi.org/10.1016/j.surfcoat.2020.126096>
  39. H.M. Zhai, H.Y. Yuan, W.S. Li, X.J. Zhang, X.S. Li, and A.H. Cai, Corrosion Resistance Mechanisms of Detonation Sprayed Fe-Based Amorphous Coating on AZ31B Magnesium Alloy, *J. Non-Cryst. Solids*, 2022, **576**(9), p 121276. <https://doi.org/10.1016/j.jnoncrysol.2021.121276>
  40. ASTM G32-16(2021) e1, *Standard Test Method for Cavitation Erosion Using Vibratory Apparatus*, American Society for Testing and Materials International, 2021.
  41. F. Bin-you, H. Ding-yong, and Z. Li-dong, Effect of Heat Treatment on the Microstructure and Mechanical Properties of Fe-Based Amorphous Coatings, *J. Alloys Compd.*, 2009, **480**(2), p 422-427. <https://doi.org/10.1016/j.jallcom.2009.02.107>
  42. Z.B. Zheng, Y.G. Zheng, W.H. Sun, and J.Q. Wang, Effect of Heat Treatment on the Structure, Cavitation Erosion and Erosion-Corrosion Behavior of Fe-Based Amorphous Coatings, *Tribol. Int.*, 2015, **90**, p 393-403. <https://doi.org/10.1016/j.triboint.2015.04.039>
  43. J. Yang, Z.B. Wang, Y.X. Qiao, and Y.G. Zheng, Synergistic Effects of Deposits and Sulfate Reducing Bacteria on the Corrosion of Carbon Steel, *Corros. Sci.*, 2022, **199**, p 110210. <https://doi.org/10.1016/j.corsci.2022.110210>
  44. H. Wang, J.H. Xu, X.S. Du, H.B. Wang, X. Cheng, and Z.L. Du, Stretchable and Self-healing Polyurethane Coating with Synergistic Anticorrosion Effect for the Corrosion Protection of Stainless Steels, *Prog. Org. Coat.*, 2022, **164**(8), p 106672. <https://doi.org/10.1016/j.porgcoat.2021.106672>
  45. F. Otsubo, H. Era, and K. Kishitake, Formation of Amorphous Fe-Cr-Mo-8P-2C Coatings by the High Velocity Oxy-Fuel Process, *J. Therm. Spray Technol.*, 2000, **9**(4), p 494-498. <https://doi.org/10.1361/105996300770349700>
  46. F. Huang, J.J. Kang, W. Yue, X.B. Liu, Z.Q. Fu, L.N. Zhu, D.S. She, G.Z. Ma, H.D. Wang, J. Liang, W. Weng, and C.B. Wang, Effect of Heat Treatment on Erosion-Corrosion of Fe-Based Amorphous Alloy Coating Under Slurry Impingement, *J. Alloys Compd.*, 2020, **820**, p 153132. <https://doi.org/10.1016/j.jallcom.2019.153132>
  47. Y. Yang, C. Zhang, Y. Peng, Y. Yu, and L. Liu, Effects of Crystallization on the Corrosion Resistance of Fe-Based Amorphous Coatings, *Corros. Sci.*, 2012, **59**, p 10-19. <https://doi.org/10.1016/j.corsci.2012.02.003>

48. D.P. Wang, S.L. Wang, and J.Q. Wang, Relationship Between Amorphous Structure and Corrosion Behaviour in a Zr-Ni Metallic Glass, *Corros. Sci.*, 2012, **59**, p 88-95. <https://doi.org/10.1016/j.corsci.2012.02.017>
49. K. Wang, S.J. Wu, Y.D. Huang, R. Wen, Y.N. Chen, D.Q. Zhou, L. Wu, J.F. Song, Z.H. Dong, and B. Jiang, Increasing the Compact Density and Its Consistency in the Cross-Section for Enhancing the Anti- corrosion and Mechanical Properties of Micro-arc Oxidation Coatings, *J. Mater. Res. Technol.*, 2022, **21**, p 1344-1352. <https://doi.org/10.1016/j.jmrt.2022.09.110>
50. D.A. Woodford, Cavitation-Erosion-Induced Phase Transformations in Alloys, *Metall. Trans.*, 1972, **3**, p 1137-1145. <https://doi.org/10.1007/bf02642445>
51. Y. Tian, H. Zhao, R. Yang, X. Liu, X. Chen, J. Qin, A. McDonald, and H. Li, In-situ SEM Investigation on Stress-Induced Microstructure Evolution of Austenitic Stainless Steels Subjected to Cavitation Erosion and Cavitation Erosion-Corrosion, *Mater. Des.*, 2022, **213**, p 110314. <https://doi.org/10.1016/j.matdes.2021.110314>
52. L. Qiao, Y.P. Wu, S. Hong, and J. Cheng, Ultrasonic Cavitation Erosion Mechanism and Mathematical Model of HVOF Sprayed Fe-Based Amorphous/Nanocrystalline Coatings, *Ultrason. Sonochem.*, 2019, **52**, p 142-149. <https://doi.org/10.1016/j.ultsonch.2018.11.010>
53. M.M. Lima, C. Godoy, P.J. Modenesi, J.C. Avelar-Batista, A. Davison, and A. Matthews, Coating Fracture Toughness Determined by Vickers Indentation: An Important Parameter in cavitation Erosion Resistance of WC-Co Thermally Sprayed Coatings, *Surf. Coat. Technol.*, 2004, **177**, p 489-496. [https://doi.org/10.1016/s0257-8972\(03\)00917-4](https://doi.org/10.1016/s0257-8972(03)00917-4)
54. A. Kanno, K. Takagi, and M. Arai, Influence of Chemical Composition, Grain Size, and Spray Condition on Cavitation Erosion Resistance of High-Velocity Oxygen Fuel Thermal-Sprayed WC Cermet Coatings, *Surf. Coat. Technol.*, 2020, **394**, p 125881. <https://doi.org/10.1016/j.surfcoat.2020.125881>
55. Y.P. Wu, S. Hong, J.F. Zhang, Z.H. He, W.M. Guo, Q. Wang, and G.Y. Li, Microstructure and Cavitation Erosion Behavior of WC-Co-Cr Coating on 1Cr18Ni9Ti Stainless Steel by HVOF Thermal Spraying, *Int. J. Refract. Met. Hard Mater.*, 2012, **32**, p 21-26. <https://doi.org/10.1016/j.ijrmhm.2012.01.002>
56. X.B. Liu, J.J. Kang, W. Yue, G.Z. Ma, Z.Q. Fu, L.N. Zhu, D.S. She, J. Liang, W. Weng, H.D. Wang, and C.B. Wang, Cavitation Erosion Behavior of HVOF Sprayed WC-10Co4Cr Cermet Coatings in Simulated Sea Water, *Ocean Eng.*, 2019, **190**, p 106449. <https://doi.org/10.1016/j.oceaneng.2019.106449>
57. C. Godoy, R.D. Mancosu, R.R. Machado, P.J. Modenesi, and J.C. Avelar-Batista, Which Hardness (Nano or Macrohardness) Should be Evaluated in Cavitation?, *Tribol. Int.*, 2009, **42**(7), p 1021-1028. <https://doi.org/10.1016/j.triboint.2008.09.007>

**Publisher's Note** Springer Nature remains neutral with regard to jurisdictional claims in published maps and institutional affiliations.

Springer Nature or its licensor (e.g. a society or other partner) holds exclusive rights to this article under a publishing agreement with the author(s) or other rightsholder(s); author self-archiving of the accepted manuscript version of this article is solely governed by the terms of such publishing agreement and applicable law.